Optics Letters

High-extinction-ratio low-voltage dual-racetrack modulator for low-power DAC-less PAM-4 modulation

Zhaobang Zeng,[1,2,3,4] **Lemeng Leng,**[1,2,3,4] **Peiyan Zhao,**[1,2,3,4] **Chenbin Zhang,**[1,2,3,4] **Ding Ding,**[1,2,3,4] **Dun Mao,**[5] **Tingyi Gu,**[5] **and Wei Jiang**[1,2,3,4,*]

[1]National Laboratory of Solid State Microstructures, Nanjing 210093, China
[2]College of Engineering and Applied Sciences, Nanjing University, Nanjing 210093, China
[3]Key Laboratory of Intelligent Optical Sensing and Manipulation (Nanjing University), Ministry of Education, Nanjing 210093, China
[4]Collaborative Innovation Center of Advanced Microstructures, Nanjing University, Nanjing 210093, China
[5]Department of Electrical and Computer Engineering, University of Delaware, Newark, Delaware 19716, USA
**Corresponding author: weijiang@nju.edu.cn*

Received 7 December 2021; accepted 6 January 2022; posted 11 January 2022; published 7 February 2022

In a parallel-coupled dual-racetrack modulator, resonant light in two resonators can interfere with each other. In lieu of critical coupling, such interference is capable of producing high extinction ratios (ERs) for high-speed modulation. Experiments demonstrate ERs of over 9 dB at 50 Gb/s and 40–50% modulation depth enhancement compared with a single-resonator modulator at 50–56 Gb/s with a peak-to-peak driving voltage of 2.3 V. Furthermore, joint modulation of two racetracks offers the possibility to combine two separate bits of driving signals to generate four-level pulse-amplitude modulation (PAM-4) without an external digital-to-analog converter (DAC). To tackle the complex multi-variable transfer function of this modulator, a procedure for configuring PAM-4 states is theoretically developed. Finally, we demonstrate 100 Gb/s PAM-4 with an electro-optic modulation power consumption of < 40 fJ/bit for this device.

https://doi.org/10.1364/OL.448441

Micro-ring modulators (MRM) are critical components in silicon photonics [1–5], owing to their compact footprint, low power consumption, and excellent wavelength selectivity [6–9]. While four-level pulse-amplitude modulation (PAM-4) first emerged in silicon traveling-wave modulators [10], PAM-4 has also been presented recently using MRMs [11–14]. Since PAM-4 modulation involves more signal levels at high speed, the limitation of the response time of MRM by the photon lifetime of the resonator [15] leads to some advanced issues. In order to obtain a wide modulation bandwidth, the MRM needs to have a moderately low Q factor, which may soften the spectral slope of the resonance dip and reduce modulation efficiency, as discussed in [8,16]. Consequently, this leads to a low modulation depth and a low extinction ratio (which is not conducive to PAM), or it requires a larger resonance shift (i.e., a larger driving voltage). Advanced coupling strategies (e.g., [16,17]) have shown great promise to potentially overcome these trade-offs in MRMs. A parallel-coupled dual racetrack resonator structure has also been proposed and simulated, albeit for quadrature amplitude modulation [18]. Such dual-racetrack modulators can also be promising candidates for alternative modulation formats such as PAM-4, which remains unexplored. Note that cascaded uncoupled MRMs have achieved DAC-less PAM-4 modulation at 60 Gb/s with <100 fJ/bit power [19]. While normal MRMs usually prefer critical coupling, a parallel-coupled dual racetrack exploiting interference in the over-coupling regime may reveal different possibilities. In this Letter, we first conduct experiments to explore the potential of a dual-racetrack modulator for fundamental binary amplitude modulation, and we find substantial enhancement of the modulation depth and extinction ratio (ER) at 50–56 Gb/s compared with single micro-ring modulators. Next, exploiting joint modulation of two interfering resonators, we show theoretically and experimentally that the dual-racetrack configuration can achieve DAC-less PAM-4 modulation at low drive voltage.

The photon transportations in the two racetracks coupled through the center waveguide (Fig. 1) can be described by multi-waveguide coupling theory and waveguide-resonator theory. For an input amplitude of unity, the output field amplitude is given by [18]

$$E_{out} = -1 + \frac{(2c_1 + 1)}{(1/2 - c_1)M + 1}, \qquad \textbf{(1)}$$

where an overall static phase factor (which is inconsequential) has been omitted and $c_1 = \frac{1}{2}\cos(\sqrt{2}\kappa L)$, with κ the coupling constant and L the coupling length of the resonators. The modulation effect arises from the resonance-dependent term

$$M(\Delta n_1, \Delta n_2) = m_1 + m_2 = \sum_{j=1,2} \{[1 - \eta_j e^{i\varphi_j + i\theta_j}]^{-1} - 1\}, \qquad \textbf{(2)}$$

where m_j represents the contribution of resonator j, η_j is the remaining amplitude fraction after a round-trip of propagation in resonator j, $\varphi_j = n_{eff} k_0 L_{tot}$ is the static round-trip phase shift, and $\theta_j = \Delta n_j k_0 L_m$ is the modulated phase. Here, Δn_j is the effective index variation in resonator j, k_0 is the free-space wavevector, L_{tot} and L_m are the circumference and length of the modulated section of each racetrack, respectively, and n_{eff} is the effective index of the waveguide. From the above equation, the variation of Δn_j in the two racetracks can change E_{out}, producing the modulation function.

0146-9592/22/040850-04 Journal © 2022 Optica Publishing Group

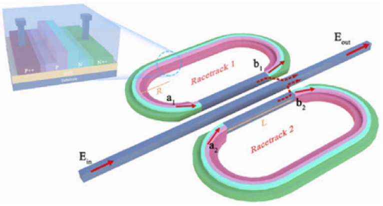

Fig. 1. Schematic drawing of the dual-racetrack modulator.

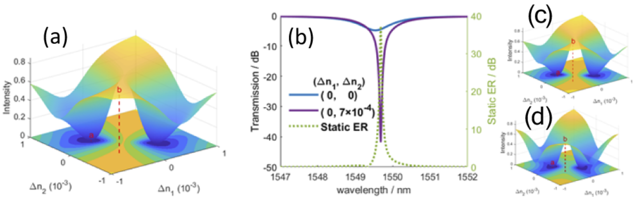

Fig. 2. (a) Simulated output intensity variation versus $(\Delta n_1, \Delta n_2)$. (b) Simulated transmission spectra and static ER as a function of wavelength for the DRM. Simulation results for (c) an increase of 50% in the Q factor of racetrack 2 or (d) a decrease in κ of 20% compared with (a).

The racetrack used here has a radius $R = 8$ μm and a straight segment length $L = 18$ μm. The gap between the resonator and the central waveguide is 0.4 μm. The thicknesses of the top silicon layer and buried oxide are 210 nm and 2 μm, respectively. A rib waveguide with a rib width of 500 nm and a 60 nm thick slab is used in the modulated section of the racetrack (multicolored region in Fig. 1). The P/N regions (doped to about $N_a = 3.5 \times 10^{18}$ cm^{-3} and $N_d = 2.5 \times 10^{18}$ cm^{-3}) comprise over 75% of the racetrack circumference. Thus, the structure has a loaded quality factor $Q \sim 4000$. The heavily doped regions are located 1 μm from the waveguide center.

Due to the refractive index changes in the two resonators, we can obtain a significant modulation of the output amplitude at resonance. The normalized output intensity I varies widely in the second and fourth quadrants of the $(\Delta n_1, \Delta n_2)$ plane in Fig. 2(a), where Δn_1 and Δn_2 have opposite signs. In particular, the modulated output amplitude E_{out} can vanish under the resonance condition $\varphi_j = 2n_j\pi$, and the modulated phase term $\theta_2 = -\theta_1 = \Delta\theta_a = \Delta n_a\, k_0\, L_m$ at point "a" in Fig. 2(a). This means that by choosing point "a" ($\Delta n_1 = -3.5 \times 10^{-4}$, $\Delta n_2 = 3.5 \times 10^{-4}$) and point "b" ($\Delta n_1 = -3.5 \times 10^{-4}$, $\Delta n_2 = -3.5 \times 10^{-4}$), a larger ER can be obtained. However, there is a problem with this for high-speed modulation: for the "a" states, $\Delta n_1 < 0$, $\Delta n_2 > 0$; hence, one of the racetracks has to work in carrier injection mode, which obviously limits the modulation speed. It would be desirable to find a set of states with all $\Delta n_j \geq 0$ (carrier depletion). To deal with this problem, we note that certain states of index modulation can be equivalently obtained by wavelength variation. Indeed, according to Eq. (2), the variation of the total phase $\varphi_j + \theta_j$ produced by $\Delta n_1 = \Delta n_2 = \Delta n_B$ is equivalent to that produced by the wavelength variation

$$\Delta\lambda_0 = \lambda_0 \Delta n_B L_m / n_{eff} L_{tot}. \tag{3}$$

This means that the modulation state for index variation $(\Delta n_1, \Delta n_2)$ at the wavelength λ_0 is equivalent to the modulation state at the wavelength $\lambda_0 + \Delta\lambda_0$ with index variation $(\Delta n_1{}^*, \Delta n_2{}^*)$, where $\Delta n_j{}^* = \Delta n_B + \Delta n_j$. Therefore, we take $\Delta n_B = 3.5 \times 10^{-4}$, and transform state "a" into "a*" ($\Delta n_1{}^* = 0$, $\Delta n_2{}^* = 7 \times 10^{-4}$) and state "b" into "b*" ($\Delta n_1{}^* = 0$, $\Delta n_2{}^* = 0$), which allows for a larger ER with all $\Delta n_j{}^* \geq 0$ (all in carrier depletion). Subsequent $\Delta n_j < 0$ cases can be treated similarly. We choose the spectra corresponding to states "a*" and state "b*." The static ER is up to 35 dB, as shown in Fig. 2(b).

Note that this dual-racetrack modulator (DRM) works in the over-coupling regime. In this regime, E_{out} generally vanishes at certain values of $(\Delta n_1, \Delta n_2)$, owing to appropriate destructive interference of the light fields from racetracks 1 and 2 back-coupled into the middle waveguide. The interference is represented by $M = m_1 + m_2$ in Eq. (2). Such interference is largely controlled by the index variation Δn_j. If fabrication variation causes parameter changes (but the system is still in the over-coupling regime), one can always adjust Δn_j to restore the desired M value to achieve $I_a = 0$ (i.e., high ER), as shown by the two examples presented in Figs. 2(c), 2(d). In contrast, high ER in a single-ring modulator relies on critical coupling, which is sensitive to fabrication variation (e.g., see the discussion in [20]) and cannot be restored by index variation.

Furthermore, we can use this structure to achieve DAC-less PAM-4 modulation, since the two resonators provide two degrees of freedom in modulation. Compared with a common Mach–Zehnder modulator or a cascaded uncoupled dual-ring modulator, the dual-racetrack modulator has a significantly more complex transfer function, which makes it non-trivial to find a proper set of PAM-4 states without a DAC. Theoretically, the key question is whether there are a set of binary index variations $\Delta n_{1,0}$ and $\Delta n_{1,1}$ for racetrack 1 and $\Delta n_{2,0}$ and $\Delta n_{2,1}$ for racetrack 2 such that the corresponding output intensity values satisfy the PAM-4 conditions. To address this question, we need to unravel the independent binary control of each bit of the PAM-4 states via Δn_1 and Δn_2.

As a first step, one can readily show from Eqs. (1) and (2) that the PAM-4 state qp (p, $q = 0, 1$) should satisfy the following equations:

$$m_{1,p} + m_{2,q} = \frac{(2c_1 + 1)}{(1/2 - c_1)(E_{qp} + 1)} - \frac{1}{1/2 - c_1}, \tag{4}$$

where E_{qp} is the output field magnitude of the PAM-4 state qp, and $m_{j,p} = m_j(\Delta n_{j,p}) = [1 - \eta_j \exp(i\Delta n_{j,p} k_0 L_m)]^{-1} - 1$ considering that $\varphi_j = 2n_j\pi$ at resonance. Note that $|E_{qp}|^2 = I_{00} + (p + 2q)\Delta I$, where I_{00} is the intensity of the state $qp = 00$ and ΔI is the intensity increment between PAM-4 states. With this form, separate binary control for bit p and bit q is now possible. Detailed analysis shows that Eq. (4) comprises four complex-valued equations (i.e., eight real-valued ones) with ten degrees of freedom, which suggests that the solution (i.e., the configuration of PAM-4 states) may not be unique. One can further show that the index variation $\Delta n_{j,p}$ can be related to the bit level change via $m_{j,p}(\Delta n_{j,p})$ in the following manner:

$$m_{1,1} - m_{1,0} = \frac{(2c_1 + 1)}{(1/2 - c_1)} \left[\frac{1}{E_{01} + 1} - \frac{1}{E_{00} + 1} \right], \tag{5}$$

$$m_{2,1} - m_{2,0} = \frac{(2c_1 + 1)}{(1/2 - c_1)} \left[\frac{1}{E_{10} + 1} - \frac{1}{E_{00} + 1} \right], \tag{6}$$

which exemplifies how $m_{1,p}$ controls the change in bit p ($E_{00} \rightarrow E_{01}$) and $m_{2,q}$ controls that the change in bit q ($E_{00} \rightarrow E_{10}$). This facilitates the search for the appropriate PAM-4 states. In practice, by storing the two 1D mappings $m_{j,p}(\Delta n_{j,p})$ in the numerical calculation, one can readily search through the combination of $m_{j,p}$ mappings to find a set of states E_{qp}, $q, p = 0, 1$ satisfying

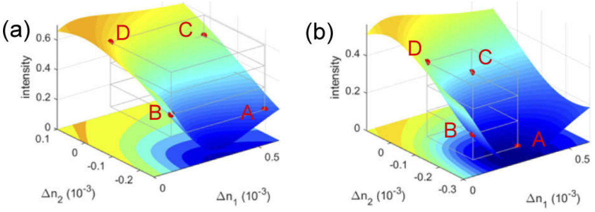

Fig. 3. Representative configurations of PAM-4 states using the DRM: (a) original structure; (b) κ decreases by 20% due to fabrication variation.

the PAM-4 requirements. Note that once the values of E_{00} and ΔI are picked, E_{10} and E_{01} can be obtained by 1D variation of m_1 or m_2 via Eqs. (5) and (6), which simplifies the search process. E_{11} can be obtained from E_{10} by varying m_1 (i.e., bit 1) via a similar equation. If the increments of $|E_{qp}|^2$ are not equal (usually due to E_{11}), one may vary E_{00} or ΔI and repeat the above procedure until the requirement is met.

Based on the above theory, one can search in any rectangular domain of the plane (Δn_1, Δn_2) in Fig. 2(a) to find PAM-4 states. Generally, for the best energy efficiency, a small variation $|\Delta n_j|$ is preferred. As the second and fourth quadrants in Fig. 2(a) have rapid intensity variations, they can produce PAM-4 states with less index variation and hence better energy efficiency. With these guidelines, we focus on the domain shown in Fig. 3(a). A representative PAM-4 configuration in this domain is depicted, with equal ΔI for states A to D. Fabrication variation may make good PAM-4 states appear in a different region, as shown in Fig. 3(b), where κ decreases 20%.

This structure is fabricated on a silicon-on-insulator wafer in a foundry. To illustrate the modulation performance enhancement, we also introduce a single-racetrack modulator (SRM) with the same structural parameters as the dual-racetrack modulator (DRM) on the same chip for comparison. Grating couplers (GCs) are used at input/output. The measured transmission spectra (normalized to the GC spectra) of the DRM and the SRM are shown in Figs. 4(a) and 4(b). Here, the fabrication-induced resonant wavelength difference between the two resonators in DRM is very small because the resonators are very close (which helps minimize fabrication non-uniformity). For the DRM, the voltages applied to racetracks 1 and 2 are defined as V_1 and V_2, respectively. The spectra indicate that the static ER of the DRM is much higher than that of the SRM.

Table 1. Comparison with Other Micro-ring Modulators

Type	V_{pp}	ER	SNR	Bit Rate
Dual-ring [21]	2 V	7.13 dB	NA	20 Gb/s
Dual-ring [17]	5 V	3.9 dB	NA	40 Gb/s
Single-ring [22]	2.5 V	4.8 dB	4.5	64 Gb/s
Single-ring [23]	2.15 V	4.6 dB	NA	50 Gb/s
Parallel DRM	2.3 V	9.4 dB	7.0	50 Gb/s

For a dynamic test, a pseudo-random binary sequence (PRBS) signal with a length of $2^{31} - 1$ is generated by a pattern generator and then amplified by a broadband amplifier (SHF 807B) to the peak-to-peak voltage $V_{pp} = 2.3$ V, with a bias tee providing a bias of −0.8 V. RF signal probes with 50 Ω terminators are used to drive the modulators. Figures 4(c)–4(f) show high-speed measurement results at optimal detuning [indicated by gray lines in Figs. 4(a), 4(b)] for the respective devices. To allow an equal comparison, only one racetrack in the DRM is driven by the signal. For the same measurement conditions, the eye opening of the DRM can be increased by 40–50% for both 50 and 56 Gbps compared with the SRM. The DRM also has a much higher signal-to-noise ratio (SNR) and ER (e.g., SNR = 6.0, ER = 7.9 dB at 56 Gb/s versus SNR = 4.0, ER = 4.6 dB for the SRM), as measured by an Agilent 86100B oscilloscope. The insertion loss ("1" level) is approximately 3.1 dB for the DRM and 3.5 dB for the SRM. The rise/fall time is 11–12 ps for the DRM, and is about 1–1.5 ps larger for the SRM, indicating they have comparable bandwidths. For further assessment, our DRM is compared with prior micro-ring modulators in Table 1. The dual-racetrack modulator reported here exhibits a markedly larger ER/SNR at high speeds (for modulators, high-speed ER is more pertinent than static ER). These results confirm that this DRM produces a high SNR and ER without demanding a high driving voltage at high speeds.

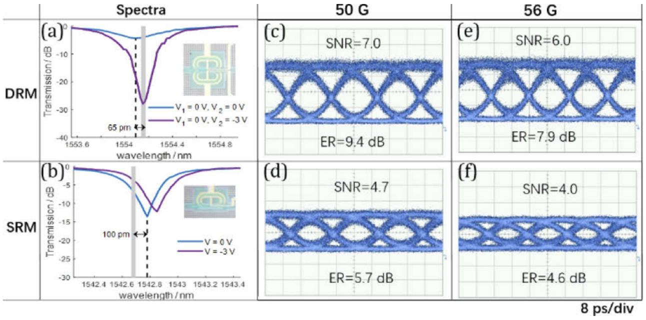

Fig. 4. Experimental transmission spectra for (a) the DRM and (b) the SRM (the inset shows optical microscope images of the devices); (c)–(f) are 50 Gb/s and 56 Gb/s eye diagrams of the SRM and the DRM.

To experimentally demonstrate the PAM-4 modulation, we use the setup shown in Fig. 5(a). First, we explore the output intensity variation with the voltage applied to two resonators at the resonant wavelength, since the index variations Δn_1 and Δn_2 correspond to the applied voltages V_1 and V_2. The voltage is scanned from −3 V to 0.5 V; a small forward bias range is used since the efficiency of changing Δn_j is maximal in this range. As the maximum forward bias here is less than the built-in potential V_{bi} (~0.99 V), the junction remains in the depletion mode without carrier lifetime concerns. The scan result is shown in Fig. 5(b). The mapping seen in Fig. 5(b) is slightly asymmetric with respect to the diagonal, which is attributed to the fabrication variation. We find the operation points A–D for DAC-less PAM-4 in Fig. 5(b), which better correspond to the states in Fig. 3(b). Thus, the two electrical signals have $V_{pp} = 2.3$ V and 1.4 V with DC biases $V_{B,1} = -1.55$ V and $V_{B,2} = -0.4$ V, respectively. Here, the insertion loss (top level) is 3.7 dB. Radio-frequency (RF) delay lines are used in each channel to synchronize the two signals. Then the driving signals are applied to the modulator using an RF probe with a GSSG (G: ground, S: signal) configuration.

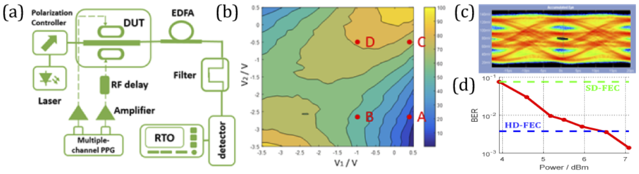

Fig. 5. PAM-4 experiment. (a) Setup. (b) Relative intensity variation with applied voltages. (c) Eye diagram of 100 Gb/s DAC-less PAM-4. (d) BER.

The output optical signal is amplified by an erbium-doped fiber amplifier (EDFA) before it is fed to a photo-detector. Finally, a real-time oscilloscope (RTO Tek DPO75902SX) is used to analyze the bit error rate (BER). Figure 5(c) presents the measured eye diagram with PRBS signals (length $2^{15}-1$), and Fig. 5(d) presents the BER versus the average power P_d at the PIN detector. The power P_d can be reduced with a more sensitive detector (e.g., an avalanche photodiode). The results demonstrate the concept of the DAC-less dual-racetrack modulator up to 100 Gb/s, while it is also possible to keep the BER below the hard-decision forward error correction (HD-FEC) threshold of 3.8×10^{-3}.

The capacitance of each racetrack modulator was calculated as 41 fF using the model in [24]. Since the power consumption of the modulator per symbol duration of modulated data is approximately $P = \frac{1}{4}CV^2$, we find that racetrack 2 consumes 20.6 fJ and racetrack 1 consumes 55.6 fJ when transmitting a symbol. As each symbol carries two bits of information, the power consumption is approximately 38 fJ/bit for this device in PAM-4 modulation, which is quite low considering that this is achieved without an electronic DAC. Note that the removal of the DAC reduces the overall cost and complexity of the system.

The PAM-4 states given by Eqs. (1), (2), and (4)–(6) provide sufficient guidance for our experiment. Dynamic modeling [4,24] of the modulator is also possible and will be reported elsewhere. If unfavorable fabrication conditions cause the resonant wavelengths λ_{j0} of the two racetracks to differ, this may induce more insertion loss, which may be recovered by thermal tuning (simulation shows a loss of approximately 10 dB for $\lambda_{10}-\lambda_{20}=0.3$ nm, which is recoverable to <2.5 dB by tuning) while retaining a high ER. Self-heating [25] or ohmic heating can induce spectral shifts in micro-resonator modulators and cause issues (e.g., pattern dependence). Here, the KP4 FEC threshold ($\sim2\times10^{-4}$) is found to be reachable using PRBS7 signals for the test reported in Fig. 5. Generally, heat-induced issues in the DRM are similar to those in the SRM. Methods such as adding negative thermo-optic materials, athermal structure designs, or controlled heaters can be used to tackle heat-induced issues [26]. Bias-voltage adjustment can also compensate for a small difference in heating between the two racetracks. Adding extra racetrack resonators to the current device may offer more latitude to optimize the device (e.g., to further increase the ER). Due to the symmetry of two resonators, a monitoring signal can be used to control two heaters with the same heating power in order to lock the two resonators, which can extend the benefit of the multi-channel simultaneous locking scheme described in Ref. [5]. Some of the performance tests discussed here are equipment limited, and could be improved with an integrated testing system that removes discrete components (e.g., RF delay lines).

In conclusion, we have designed and demonstrated a parallel-coupled dual-racetrack modulator with a high extinction ratio (over 20 dB statically and over 9 dB at 50 Gb/s) and high SNR. By modulating the refractive index of the silicon waveguide in the two parallel-coupled resonators, 100 Gb/s PAM-4 modulation can be obtained without electronic DAC assistance. Such a compact, high-ER, low-voltage modulator may open up new possibilities for a multitude of chip-scale applications (e.g., [15]).

Funding. National Natural Science Foundation of China (61775094); Jiangsu Innovation Team; National Key Research and Development Program of China (2017YFA0303700); Defense Advanced Research Projects Agency (N66001-21-1-4034).

Disclosures. The authors declare no conflicts of interest.

Data availability. Data underlying the results presented herein are not publicly available at this time but may be obtained from the authors upon reasonable request.

REFERENCES

1. T. Y. Liow, K. W. Ang, Q. Fang, J. F. Song, Y. Z. Xiong, M. B. Yu, G. Q. Lo, and D. L. Kwong, IEEE J. Sel. Top. Quantum Electron. **16**, 307 (2010).
2. D. A. B. Miller, Proc. IEEE **97**, 1166 (2009).
3. G. T. Reed, G. Mashanovich, F. Y. Gardes, and D. J. Thomson, Nat. Photonics **4**, 661 (2010).
4. W. D. Sacher and J. K. S. Poon, Opt. Lett. **34**, 3878 (2009).
5. P. Dong, R. Gatdula, K. Kim, J. H. Sinsky, A. Melikyan, Y.-K. Chen, G. de Valicourt, and J. Lee, Opt. Express **25**, 16040 (2017).
6. Q. F. Xu, B. Schmidt, S. Pradhan, and M. Lipson, Nature **435**, 325 (2005).
7. C. Li, L. J. Zhou, and A. W. Poon, Opt. Express **15**, 5069 (2007).
8. Y. Li, L. Zhang, M. Song, B. Zhang, J.-Y. Yang, R. G. Beausoleil, A. E. Willner, and P. D. Dapkus, Opt. Express **16**, 13342 (2008).
9. R. Yang, L. Zhou, H. Zhu, and J. Chen, Opt. Express **23**, 28993 (2015).
10. C. Xiong, D. M. Gill, J. E. Proesel, J. S. Orcutt, W. Haensch, and W. M. J. Green, Optica **3**, 1060 (2016).
11. R. Dubé-Demers, S. LaRochelle, and W. Shi, Optica **3**, 622 (2016).
12. Y. Yuan, W. V. Sorin, Z. Huang, D. Liang, M. Fiorentino, and R. G. Beausoleil, in *IEEE Photonics Conference (IPC)* (2021), WG2.
13. R. Li, D. Patel, A. Samani, E. El-Fiky, Z. Xing, M. Morsy-Osman, and D. V. Plant, IEEE Photonics Technol. Lett. **29**, 1046 (2017).
14. M. S. Hai, M. M. P. Fard, and O. Liboiron-Ladouceur, IEEE J. Sel. Top. Quantum Electron. **22**, 123 (2016).
15. C. Sun, M. T. Wade, Y. Lee, J. S. Orcutt, L. Alloatti, M. S. Georgas, A. S. Waterman, J. M. Shainline, R. R. Avizienis, S. Lin, B. R. Moss, R. Kumar, F. Pavanello, A. H. Atabaki, H. M. Cook, A. J. Ou, J. C. Leu, Y. H. Chen, K. Asanovic, R. J. Ram, M. A. Popovic, and V. M. Stojanovic, Nature **528**, 534 (2015).
16. R. A. Cohen, O. Amrani, and S. Ruschin, Nat. Photonics **12**, 706 (2018).
17. Y. Hu, X. Xiao, X. H. Xu, X. Li, K. Xiong, Z. Li, T. Chu, Y. Yu, and J. Yu, Opt. Express **20**, 15079 (2012).
18. R. A. Integlia, L. Yin, D. Ding, D. Z. Pan, D. M. Gill, and W. Jiang, Opt. Express **19**, 14892 (2011).
19. R. Dubé-Demers, S. LaRochelle, and W. Shi, Opt. Lett. **41**, 5369 (2016).
20. P. Chen, S. Chen, X. Guan, Y. Shi, and D. Dai, Opt. Lett. **39**, 6304 (2014).
21. T. Gu, Y.-K. Chen, C. W. Wong, and P. Dong, Opt. Lett. **39**, 4974 (2014).
22. J. Sun, R. Kumar, M. Sakib, J. B. Driscoll, H. Jayatilleka, and H. S. Rong, J. Lightwave Technol. **37**, 110 (2019).
23. S. Pitris, M. Moralis-Pegios, T. Alexoudi, K. Fotiadis, Y. Ban, P. De Heyn, J. V. Campenhout, and N. Pleros, in *Optical Fiber Communication Conference (OFC)* (2020), M4H.3.
24. R. Dubé-Demers, J. St-Yves, A. Bois, Q. Zhong, M. Caverley, Y. Wang, L. Chrostowski, S. LaRochelle, D. V. Plant, and W. Shi, J. Lightwave Technol. **33**, 4240 (2015).
25. M. J. Shin, Y. Ban, B. Yu, J. Rhim, L. Zimmermann, and W. Choi, IEEE J. Sel. Top. Quantum Electron. **22**, 116 (2016).
26. K. Padmaraju and K. Bergman, Nanophotonics **3**, 269 (2014).